doi:10.1093/jmcb/mjz076
Published online July 23, 2019

Article

Neogenin-loss in neural crest cells results in persistent hyperplastic primary vitreous formation

Sen Lin[1,2,†], Wei Liu[1,2,†], Chun-Lin Chen[1,2,†], Dong Sun[1,3], Jin-Xia Hu[1], Lei Li[1], Jian Ye[2], Lin Mei[1,3], and Wen-Cheng Xiong[1,3,*]

[1] Department of Neuroscience & Regenerative Medicine and Department of Neurology, Augusta University, Augusta, GA 30912, USA
[2] Department of Ophthalmology, Daping Hospital, Army Medical Center of PLA, Chongqing, China
[3] Department of Neurosciences, School of Medicine, Case Western Reserve University, Cleveland, OH 44106, USA
[†] These authors contributed equally to this work.
* Correspondence to: Wen-Cheng Xiong, E-mail: wen-cheng.xiong@case.edu

Edited by Zhen-Ge Luo

Neogenin is a transmembrane receptor critical for multiple cellular processes, including neurogenesis, astrogliogenesis, endochondral bone formation, and iron homeostasis. Here we present evidence that loss of neogenin contributes to pathogenesis of persistent hyperplastic primary vitreous (PHPV) formation, a genetic disorder accounting for ~5% of blindness in the USA. Selective loss of neogenin in neural crest cells (as observed in *Wnt1*-Cre; *Neo*$^{f/f}$ mice), but not neural stem cells (as observed in *GFAP*-Cre and *Nestin*-Cre; *Neo*$^{f/f}$ mice), resulted in a dysregulation of neural crest cell migration or delamination, exhibiting features of PHPV-like pathology (e.g. elevated retrolental mass), unclosed retinal fissure, and microphthalmia. These results demonstrate an unrecognized function of neogenin in preventing PHPV pathogenesis, implicating neogenin regulation of neural crest cell delamination/migration and retinal fissure formation as potential underlying mechanisms of PHPV.

Keywords: neogenin, PHPV, ocular fissure, neural crest cells

Introduction

Persistent hyperplastic primary vitreous (PHPV), a potentially blinding childhood disease, is one of the most common congenital malformation syndromes of the eye. PHPV pathology usually occurs unilaterally, but a rare bilateral condition has also been described (Goldberg, 1997; Sanghvi et al., 2005; Rizvi et al., 2013). Although intraocular lens implantation and surgical intervention have been used to prevent PHPV-induced progressive glaucoma and pupillary blockage (Goldberg, 1997; Pollard, 1997; Anteby et al., 2002; Hunt et al., 2005), the outcome of PHPV is barely satisfactory. Furthermore, the cellular and molecular mechanisms responsible for the development of PHPV remain largely unclear.

During eye development a transient capillary network hyaloid vascular system (HVS) forms around the fourth to seventh week of human fetal life (Shirai, 1991; Gulati et al., 2003), providing nutrition to the developing lens, vitreous, and retina before the intraretinal vasculature is formed (Goldberg, 1997; Ito and Yoshioka, 1999). During later stages of mammalian eye development, the HVS undergoes dramatic involution (in humans, by embryonic week 20; in mouse, by E13.5) (Ito and Yoshioka, 1999; Gulati et al., 2003). Failed HVS regression results in congenital malformation of human eye disease known as PHPV (Pollard, 1997; Shastry, 2009). Previous studies with ochratoxin A have demonstrated abnormal migration of excessive mesenchymal cells in PHPV tissues in both eyes, containing melanocytes derived from the neural crest (Beauchamp and Knepper, 1984; Matsubara et al., 2001). Moreover, fate maps developed in quail chick chimeras have demonstrated that periocular mesenchyme contains initial cell linages from both the neural crest and the mesoderm (Johnston et al., 1979; Le Douarin, 1980; Kulesa et al., 2004). Subsequently, abnormal development of neural crest cells (NCCs) during embryonic fissure closure (4–7 weeks of gestation) can result in Peters' anomaly, PHPV, and other ocular malformations (Matsubara et al., 2001).

Multiple signaling pathways have been reported to be involved in PHPV formation, which include proto-oncogene *ski* (McGannon et al., 2006), tumor suppressor gene *Arf* (McKeller

Received December 6, 2018. Revised March 7, 2019. Accepted June 12, 2019.

et al., 2002; Martin et al., 2004; Thornton et al., 2007; Freeman-Anderson et al., 2009), *p53* (Reichel et al., 1998), *Frizzled-5* (Zhang et al., 2008), *ATOH7* (Prasov et al., 2012), *ang-2* (Hackett et al., 2002), *Bax* and *Bak* (Hahn et al., 2005), *FZD4* (Shastry, 2009; Kheir et al., 2016), *LRP5* (Shastry, 2009; Kheir et al., 2016), *ephrin-B2* (Salvucci et al., 2015), and *ephrin-A5* (Son et al., 2014). Despite the fact that NCC input contributes to the detrimental, redundant retrolental mass via an unclosed ocular fissure, the relationship between fissure closure and PHPV is yet to be defined.

Neogenin is initially identified as a DCC (deleted in colon cancer) family receptor, which binds to axon guidance cues of netrins and RGMs, implicated in axon pathfinding (Monnier et al., 2002; Wilson and Key, 2006; De Vries and Cooper, 2008; Xu et al., 2014). Neogenin also acts as a co-receptor for bone morphogenetic proteins (BMPs), involved in BMP regulated iron homeostasis, astrogliogenesis, and endochondrial bone formation (Lee et al., 2010; Zhou et al., 2010; Huang et al., 2016). Recently, neogenin is found to be a key regulator of adult hippocampal neurogenesis (Sun et al., 2018). Neogenin is highly expressed in embryonic retina, exhibiting a temporal–nasal expression pattern (Rajagopalan et al., 2004; Schnichels et al., 2007), where it is implicated in regulating retinal axonal pathfinding. However, the exact role of neogenin in retina/eye development remains largely unclear.

Here we provide evidence that loss of neogenin contributes to the formation of PHPV. Neogenin is highly expressed in NCCs in developing embryos. Conditionally knocking out (cKO) neogenin in NCCs (by *Wnt1*-Cre) resulted in PHPV-like phenotype. Further characterizing phenotypes in neogenin cKO embryos and in NCC cultures revealed retinal fissure closure deficit and altered NCCs migration. These observations suggest that neogenin in NCCs is necessary to prevent PHPV pathogenesis, which is likely due to neogenin's functions in regulating NCC delamination/migration and retinal fissure closure.

Results

PHPV-like pathology in Neo$^{m/m}$ mice

To investigate neogenin's function in mouse retina, we took advantage of *Neo*$^{m/m}$ mice, a hypomorphic allele with ~90% loss of neogenin as described previously (Lee et al., 2010), and examined their eye phenotypes. *Neo*$^{m/m}$ mice die around P28 (Lee et al., 2010). Thus, the whole-mount and histologic investigations of postnatal (P) eyes at ages of P1, P7, P20, and P30 from *Neo*$^{m/m}$ and their littermate control (*Neo*$^{+/+}$ and *Neo*$^{+/m}$) pups were carried out. Remarkably, a large pigmented mass was identified in all ages of *Neo*$^{m/m}$ eye, which encapsulated vasculature posterior to the lens and extended toward the retina in a funnel-like shape (Figure 1A and B), indicative of a pathologic feature of PHPV (Haddad et al., 1978; Cooper et al., 2008; Zhang et al., 2008; Jun et al., 2009). *Neo*$^{m/m}$ eye also exhibited several additional hallmark characteristics of PHPV, including retinal atrophy or smaller eye (microphthalmia; Figure 1A and B; Supplementary Table S1), catarods (data not shown). These phenotypes were detectable in ~100% of the mutant eyes in all postnatal ages examined.

Normal hyaloid vessel regression in postnatal Neo$^{m/m}$ mice

Previous studies have indicated that PHPV may result from a failure regression of the hyaloid vessels (Goldberg, 1997; Pollard, 1997; Shastry, 2009). We thus examined hyaloid vessels surrounding lens of *Neo*$^{+/+}$ and *Neo*$^{m/m}$ mice at ages of P1, P7, and P14 by Isolectin B4 staining (Figure 2A). *Neo*$^{m/m}$ eyes exhibited slightly more hyaloid vessels than that of *Neo*$^{+/+}$ littermate controls at ages of P1 (Figure 2A and B). However, at age of P7 and P14, marked reductions in hyaloid vessels were observed in both *Neo*$^{+/+}$ and *Neo*$^{m/m}$ mice, and no significant difference of hyaloid vessel density was detectable between *Neo*$^{+/+}$ and *Neo*$^{m/m}$ mice (Figure 2A and B). At age of P14, the ratio of retrolental mass area over lens area was lower than that observed at P7 (Figure 2C). These observations are in line with the view that mouse hyaloid vessels normally regress during the first two weeks of postnatal development (Ito and Yoshioka, 1999), and suggest that the PHPV-like phenotype in *Neo*$^{m/m}$ may not due to a defective postnatal hyaloid vessel regression, but is likely to be resulted from a defect during embryonic development.

Retrolental mass in Neo$^{m/m}$ embryos with characteristics of neural crest origin

We then investigated embryonic phenotypes in *Neo*$^{m/m}$ mice. As shown in Figure 3A–C, hematoxylin and eosin (H&E) staining analysis of *Neo*$^{+/+}$ and *Neo*$^{m/m}$ embryonic sections (E11.5–E14.5) showed slight increases in area of cell mass retrolentally. At E16.5, a marked increase in retrolental cell mass was detected in the mutant eye (Figure 3D and E). These results suggest that the retrolental cells may start their regression in *Neo*$^{+/+}$ eye, but not *Neo*$^{m/m}$ eye, after E14.5. The increase in retrolental cell mass in E10.5 mutant eye was not due to increased cell proliferation, as no significant difference in Ki67-positive cells over 4',6-diamidino-2-phenylindole (DAPI)-positive cells was detected between *Neo*$^{+/+}$ and *Neo*$^{m/m}$ eyes at E10.5 (Figure 3F). However, Ki67-positive cells were higher in the retrolental mass in E16.5 *Neo*$^{m/m}$ vitreous compared with that in *Neo*$^{+/+}$ eyes (Figure 3G), suggesting a possible cellular mechanism for the elevated retrolental cell mass in E16.5 mutant embryos.

The retrolental vitreous contains elements of the hyaloid vessels, which are composed of endothelial cells and other types of perivascular cells (Ito and Yoshioka, 1999; Zhu et al., 1999; Son et al., 2014). These cells are believed largely derived from neural crest origin (Barishak, 1992; Son et al., 2014). We thus immunostained control and mutant embryos with antibodies against PDGFRβ, CD31, AP2β, and MiTF, markers for pericytes, endothelial cells, NCCs, and melanocyte precursors, respectively. In comparison to E12.5 *Neo*$^{+/+}$ embryos, more PDGFRβ-positive cells (pericytes) were emerged in the vitreous of the *Neo*$^{m/m}$ eye (Figure 4A–C). In addition, AP2β^{+} NCCs were higher in the mutant eye (Figure 4A and C). We also found abundant CD31-positive cells in the vitreous of *Neo*$^{+/+}$ and *Neo*$^{m/m}$ eye (Figure 4D–F), and limited number of NG2-positive cells (for pericytes marker; Figure 4D and F) only in *Neo*$^{m/m}$, but not *Neo*$^{+/+}$ eyes (Figure 4D and F). Furthermore, there was a greater prevalence of AP2β-positive cells in the vitreous of the

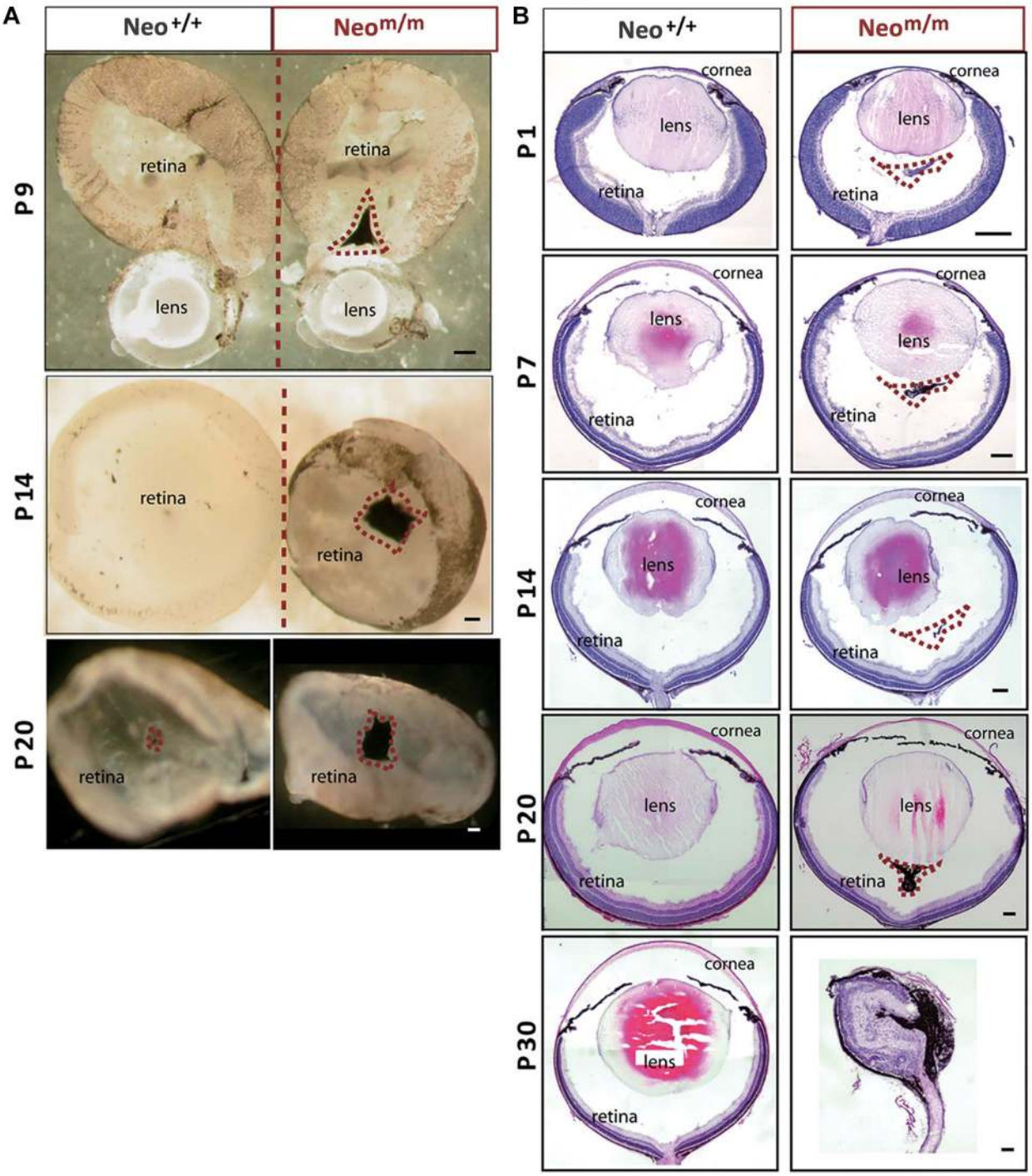

Figure 1 *Neo*$^{m/m}$ mice develop symptoms of PHPV and permanent retrolental cell mass. (**A**) In a retinal whole-mount view (P9, P14, and P20), the retrolental mass located behind the lens and attached to the retina exhibit pigment cell characteristics. Scale bar, 500 µm. (**B**) Histologic sections of *Neo*$^{+/+}$ and *Neo*$^{m/m}$ mice at P1, P7, P14, and P30, the retrolental mass exist in *Neo*$^{m/m}$ vitreous during life time (*Neo*$^{m/m}$ mice only have a lifespan around P30). At P30 the *Neo*$^{m/m}$ eye showed microphthalmia phenotype of which the pigment cell invaded into the inner eye tissues, such as retina. Scale bar, 500 µm.

Neo$^{m/m}$ eye at E12.5 compared to the *Neo*$^{+/+}$ eye (Figure 4A–C). MiTF-positive cells were found residing in the vitreous of the *Neo*$^{m/m}$, but not *Neo*$^{+/+}$, eye as early as E14.5 (Figure 4G–I). To further identify the origin of the cells in retrolental mass, we used Sox9, FoxD3, and Sox10 antibodies to label migratory NCCs Kim et al., 2003; Mori-Akiyama et al., 2003; (Kelsh, 2006; Teng et al., 2008; Wang et al., 2011). In comparison to E12.5 *Neo*$^{+/m}$ embryos, more Sox9 immuno-positive cells (Sox9^{+}) were found

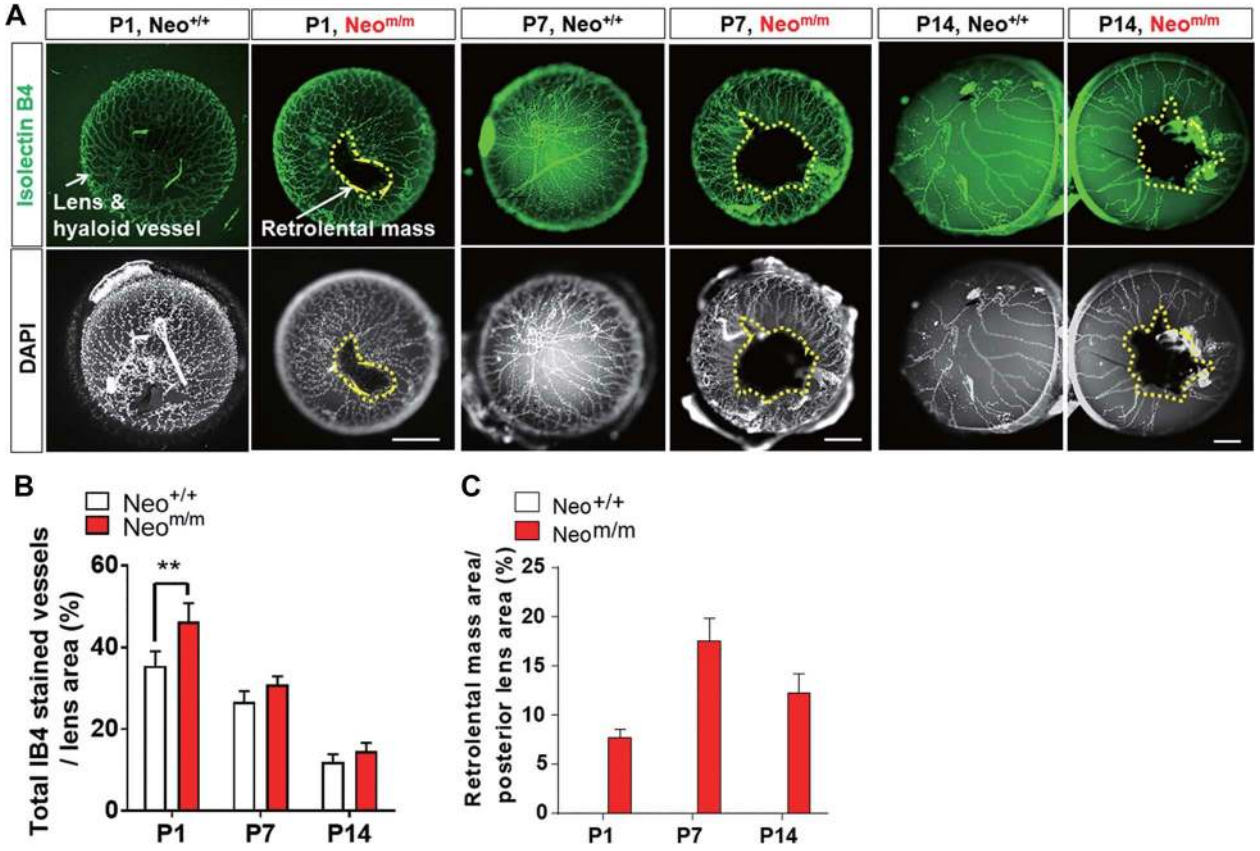

Figure 2 Hyaloid vessel structures regressed in area outside retrolental mass within *Neo*$^{m/m}$ eye after birth. (**A**) Whole-mount preparation of lenses detected from the posterior of *Neo*$^{+/+}$ and *Neo*$^{m/m}$ eyes at several postnatal stages. Lenses were dissected with hyaloid vessels intact and retrolental mass attached, and stained with fluorescein isothiocyanate (FITC)-conjugated isolectin-B4. The retrolental mass was highlighted by a yellow-dotted line. Scale bar, 500 μm. (**B**) Quantification of vessel density (vessel area vs. posterior lens area) at several postnatal stages in *Neo*$^{+/+}$ and *Neo*$^{m/m}$ eyes. Hyaloid vessel regression was observed both in *Neo*$^{+/+}$ and *Neo*$^{m/m}$ eyes. $n = 7$, $^{**}P < 0.01$. (**C**) Quantification of retrolental mass density (retrolental mass area vs. posterior area) at different postnatal stages.

inside the *Neo*$^{m/m}$ eyes, and more Sox9^{+} cells outside the eye disc (Figure 4K and L), but no significant difference of Sox9^{+} cell ratio (retrolental/outside eye disc) was found between the two groups (Figure 4M). As for FoxD3, neither the significant difference of number of FoxD3^{+} cells were found inside and outside the eye discs, nor the ratio (Figure 4J, N, O and P). However, abundant Sox10^{+} cells were emerged in the vitreous and fissure of *Neo*$^{m/m}$ eyes rather than the *Neo*$^{+/m}$ groups. No difference of number of Sox10^{+} cells was found outside the eye disc; thus, the Sox10^{+} cell ratio increased in *Neo*$^{m/m}$ group (Figure 4J, Q, R and S).

Expression of neogenin in neural crest-lineage cells

To understand how neogenin-loss results in PHPV-like phenotype, we examined neogenin's expression pattern in developing eye. In *Neo*$^{m/m}$ mice, a LacZ gene is inserted into the intron of neogenin gene, and thus the LacZ expression/activity is under the control of neogenin promotor (Zhou et al., 2010). We thus used this LacZ as a reportor for neogenin's expression. As shown in Figure 5A, LacZ activity was undetectable in *Neo*$^{+/+}$ control embryos, but it was obvious in *Neo*$^{+/m}$ and *Neo*$^{m/m}$ retinal sections, demonstrating the specificity. The LacZ signal was weakly detected in ~E11 eye cup (Figure 5A), but was strong in ~E13.5 or late stage eye cups of *Neo*$^{m/m}$ embryos (Figure 5A). In E15.5 *Neo*$^{m/m}$, LacZ was distributed in neuroretina, lens epithelium, eye stalk, periocular mesenchyme, putative cornea, vitreous, and RPE (Figure 5A). In P9 *Neo*$^{m/m}$, LacZ was expressed in the ganglion cell layer, inner nuclear layer, retrolental mass, and RPE (Figure 5A). Importantly, LacZ^{+} signals were detectable in the retrolental cell masses in *Neo*$^{m/m}$, but not *Neo*$^{+/+}$ retina, at ages of E15.5 and P9 (Figure 5A). We next determined if these LacZ^{+} cells are NCCs or derived from NCCs. Co-immunostaining analysis using antibodies against β-gal with anti-AP2β (a marker for NCCs), anti-PDGFRβ (a marker for pericytes), or anti-MiTF (a marker for melanocyte precursors) revealed co-distribution of LacZ^{+}Ap2β^{+} and LacZ^{+}PDGFβ^{+} cells (Figure 5B), suggesting that neogenin is highly expressed in AP2β^{+} NCCs and NCC derived PDGFβ^{+} pericytes. MiTF^{+}LacZ^{+} cell was seldom observed (Figure 5C and C1), and few CD31^{+} cells were co-labeled with LacZ (Figure 5C and C2), in line with the view for neogenin's expression largely in NCCs (Figure 5D).

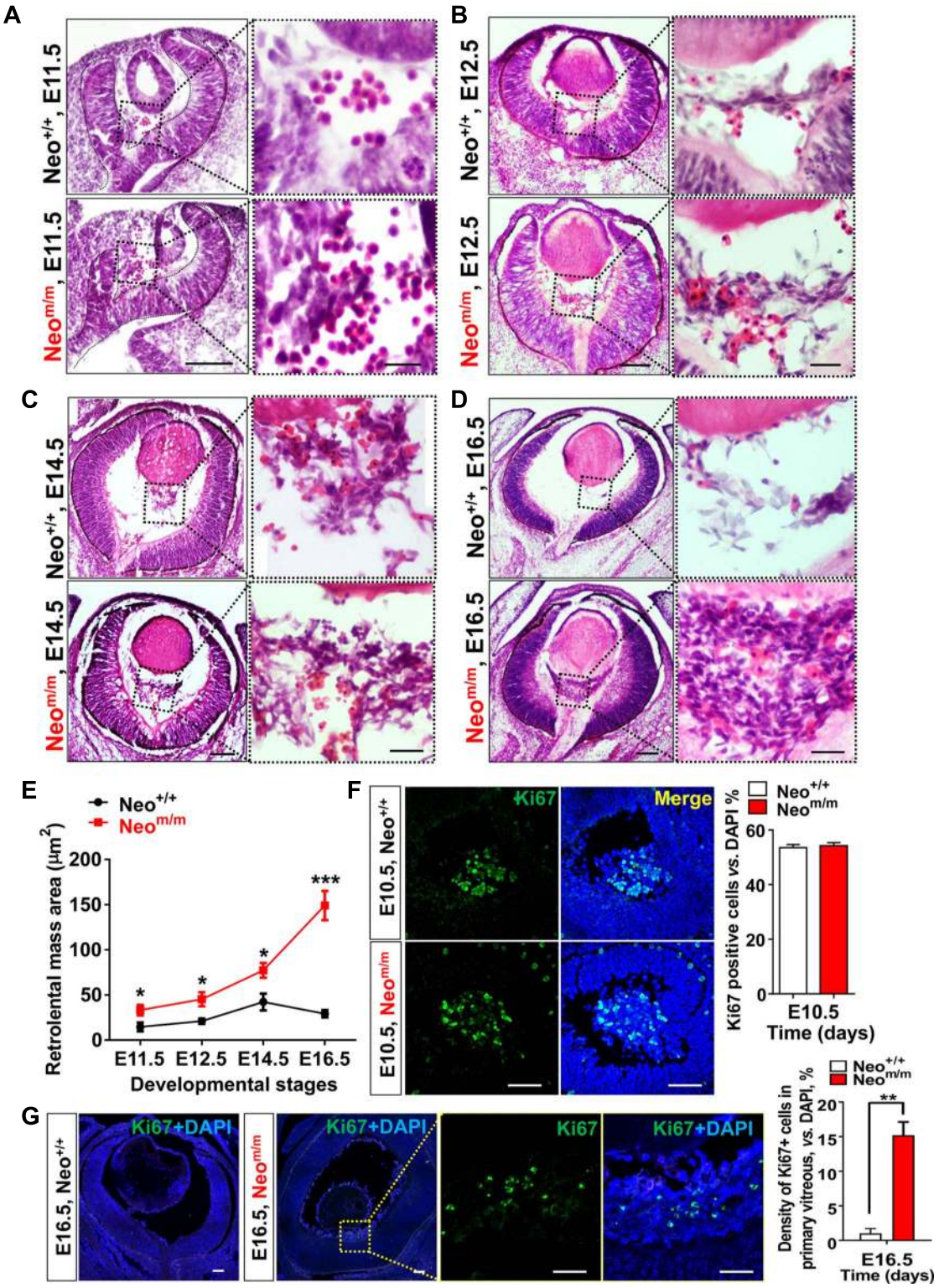

Figure 3 The persistent primary vitreous in the *Neo*$^{m/m}$ mice originated from the beginning of eye cup formation and increased in volume during ocular development. (**A**–**D**) H&E staining of embryonic eye cup in coronal plane at E11.5, E12.5, E14.5, and E16.5. Scale bar, 100 μm. Enlarged scale bar, 25 μm. (**E**) Quantitative analysis of retrolental mass area (μm^2) in **A**–**D**. $n = 7$, $^*P < 0.05$, $^{***}P < 0.001$. Data as mean ± SEM. Student's *t*-test. (**F**) Ki67 immunostaining of *Neo*$^{+/+}$ and *Neo*$^{m/m}$ eye cup at E10.5. Quantification of Ki67-positive cells vs. DAPI-positive cells. No significant difference. $n = 4$. Scale bar, 50 μm. (**G**) Ki67 immunostaining of eye cup at E16.5. Enlarged area indicates the retrolental mass. Quantification of Ki67-positive cells vs. DAPI-positive cells. Significant difference. $n = 4$. Scale bar, 50 μm.

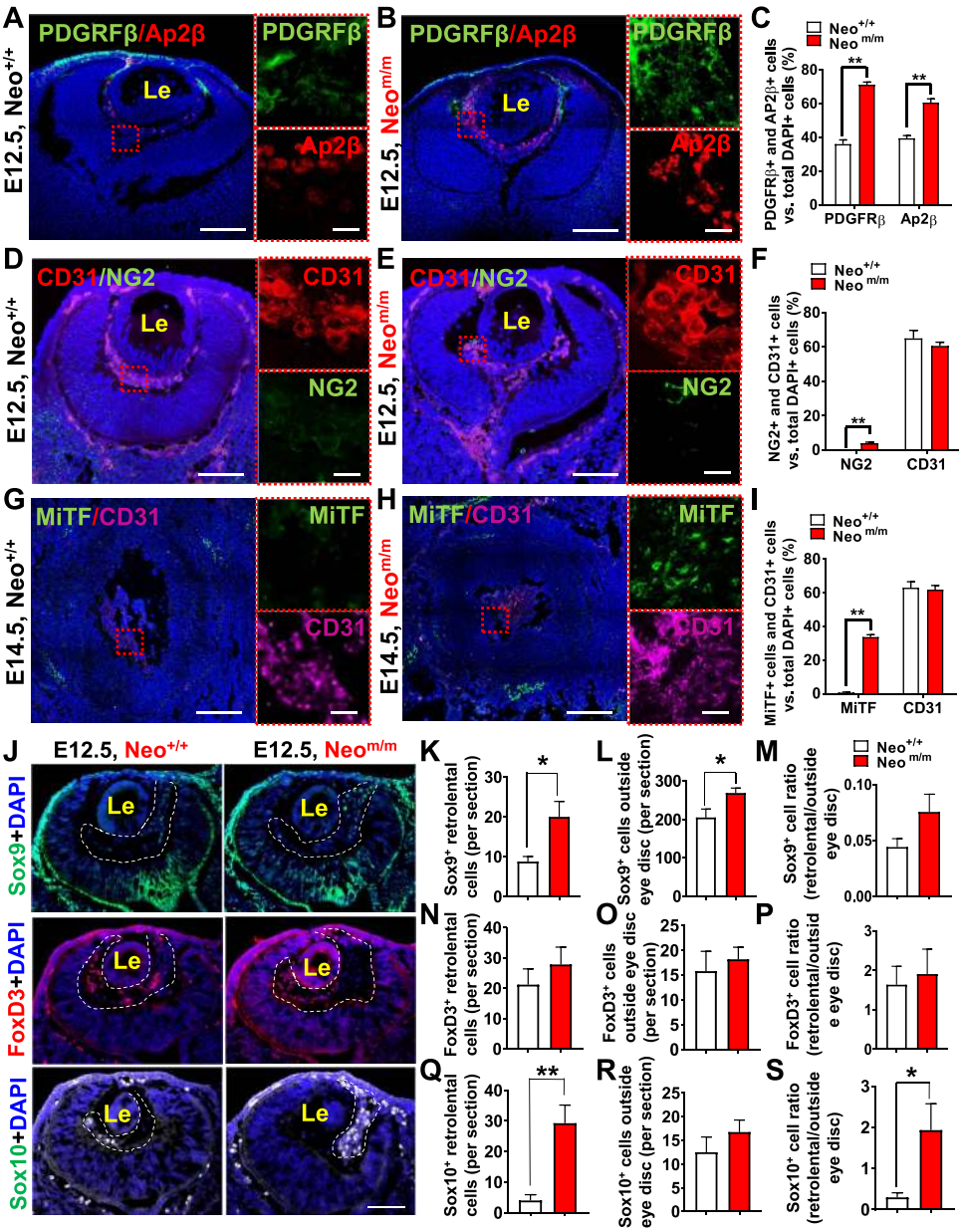

Figure 4 *Neo*$^{m/m}$ vitreous contains more pericytes, endothelial cells, melanocyte precursors, and blood cells, and increase of NCCs in E12.5 *Neo*$^{m/m}$ embryos. (**A** and **B**) PDGFRβ (green) and AP2β (red) expressed in the vitreous of *Neo*$^{+/+}$ and *Neo*$^{m/m}$ mice at E12.5. The red-dotted boxes are highlighted as separated figures along the right side. Scale bar, 100 and 10 μm (enlarged). (**C**) Quantification of PDGFRβ (green) and AP2β (red)-positive area vs. DAPI area (%). (**D** and **E**) CD31 (red) and NG2 (green) expressed in the vitreous of *Neo*$^{+/+}$ and *Neo*$^{m/m}$ mice at E12.5. The red-dotted boxes are highlighted as separated figures along the right side. Scale bar, 100 and 10 μm (enlarged). (**F**) Quantification of CD31 (red) and NG2 (green)-positive area vs. DAPI area (%). (**G** and **H**) MiTF-positive cells emerged at E14.5. The red-dotted boxes are highlighted as separated figures along the right side (MiTF, green; CD31 purple). Scale bar, 100 and 10 μm (enlarged). (**I**) Quantification of CD31 and MiTF-positive area vs. DAPI area (%). $n = 4$ eyes, 3 sections each eye, $^{**}P < 0.01$. (**J**) Immunostaining of Sox9 (green), FoxD3 (red) and Sox10 (white) in eyes of E12.5 *Neo*$^{+/+}$ and *Neo*$^{m/m}$ embryos. Scale bar, 100 μm. (**K**–**M**) Quantitative analysis of the Sox9$^+$ cells (**K**, Sox9$^+$ retrolental cells; **L**, Sox9$^+$ cells surrounding eye disc; **M**, the ratio of Sox9$^+$ retrolental cells over Sox9$^+$ cells surrounding eye disc) in E12.5 *Neo*$^{+/+}$ and *Neo*$^{m/m}$ embryos. (**N**–**P**) Quantitative analysis of the FoxD3$^+$ cells (**N**, FoxD3$^+$ retrolental cells; **O**, FoxD3$^+$ cells surrounding eye disc; **P**, the ratio of FoxD3$^+$ retrolental cells over FoxD3$^+$ cells surrounding eye disc) in E12.5 *Neo*$^{+/+}$ and *Neo*$^{m/m}$ embryos. (**Q**–**S**) Quantitative analysis of the Sox10$^+$ cells (**Q**, Sox10$^+$ retrolental cells; **R**, Sox10$^+$ cells surrounding eye disc; **S**, the ratio of Sox10$^+$ retrolental cells over Sox10$^+$ cells surrounding eye disc) in E12.5 *Neo*$^{+/+}$ and *Neo*$^{m/m}$ embryos. $n = 3$ per group. Data are mean ± SEM. Student's *t*-test. $^*P<0.05$, $^{**}P<0.01$, in comparison with control group.

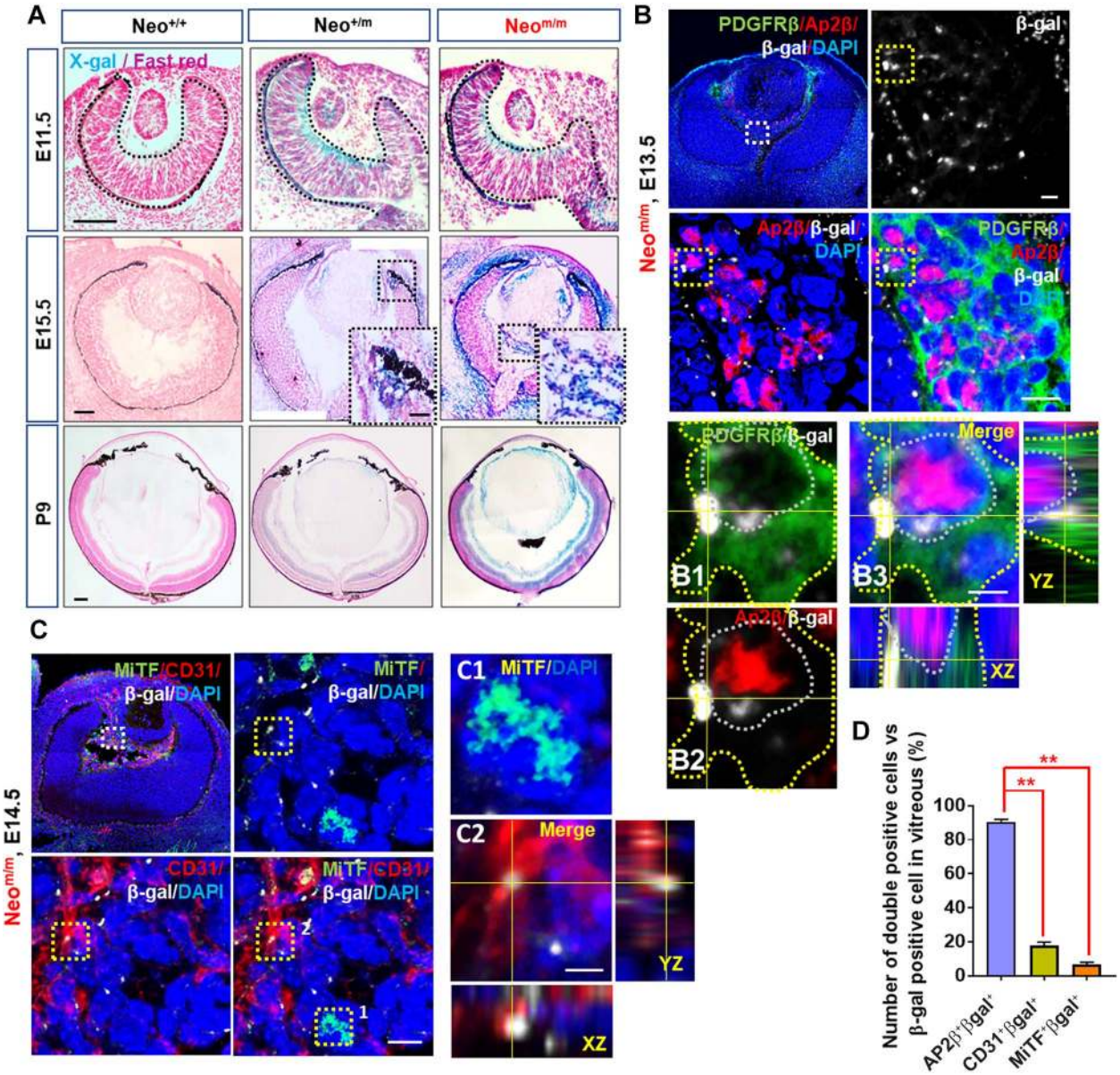

Figure 5 Co-localization of neogenin at different embryonic stages. (**A**) Coronal sections of E11.5, E15.5, and P9 eye cups in *Neo*$^{+/+}$, *Neo*$^{+/m}$, and *Neo*$^{m/m}$ were co-stained by X-gal and fast red. Scale bar, 100 μm. X-gal staining in coronal and sagittal sections at E15.5. X-gal signals were found expressed in the perioclular mesenchyme, retrolental mass, and lens epithelium. Scale bar, 100 and 25 μm (enlarged). (**B**) Expression of PDGFRβ and Ap2β co-localized with β-gal, which is the puncta shape (white dot) in the vitreous. (**B1**–**B3**) Yellow-dotted areas are highlighted images. Scale bar, 10 μm. (**C**) β-Gal (white) co-labeled with PDGFRβ (green) and Ap2β (red) located in the perinuclear region. AP2β expressed in the nucleus (red) co-labeled with DAPI. In the merged figure, the YZ and XZ axis view show the co-localization of AP2β, PDGFRβ, β-gal, and DAPI. β-gal is located just in the perinuclear region. Scale bar, 2.5 μm. (**C1**) MiTF (green) and CD31 (red) expression co-localized with β-gal, puncta shape (white dot) in the vitreous. Scale bar, 10 μm. (**C2**) β-gal (white) did not co-labeled with CD31 (red). MiTF (green) expressed in the nucleus (red) co-labeled with DAPI but not β-gal (white). In the merged figure, the YZ and XZ axis view shows β-gal co-localized with CD31, but not MiTF. Scale bar, 2.5 μm. (**D**) Quantification of the double immuno-positive cells vs. β-gal^{+} cells in the vitreous of *Neo*$^{m/m}$ eye cup at E13.5 and E14.5. By co-staining we observed β-gal colabeling with 90.5% ± 3.8% of AP2β-positive cells, 17.8% ± 4.9% of CD31-positive cells, 6.5% ± 3.7% of MiTF-positive cells, and 91.7% ± 3.8% of PDGFRβ-positive cells. $n = 6$, $^{**}P < 0.01$. Student's *t*-test.

PHPV-like pathology in NCC neogenin cKO mice, Neo$^{f/f}$*;Wnt1-Cre mice*

We then examined whether loss of neogenin in NCCs contributes to the PHPV-like pathology. To this end, we crossed *Neo*$^{f/f}$ with *Wnt1*-Cre to generate NCC selective neogenin cKO mice, *Neo*$^{f/f}$;*Wnt1*-Cre mice, as *Wnt1*-Cre expresses Cre selectively in NCC lineage cells (Brault et al., 2001; Chen et al., 2006; Taylor et al., 2007). Indeed, *Neo*$^{f/f}$;*Wnt1*-Cre, but not control (*Neo*$^{f/f}$)

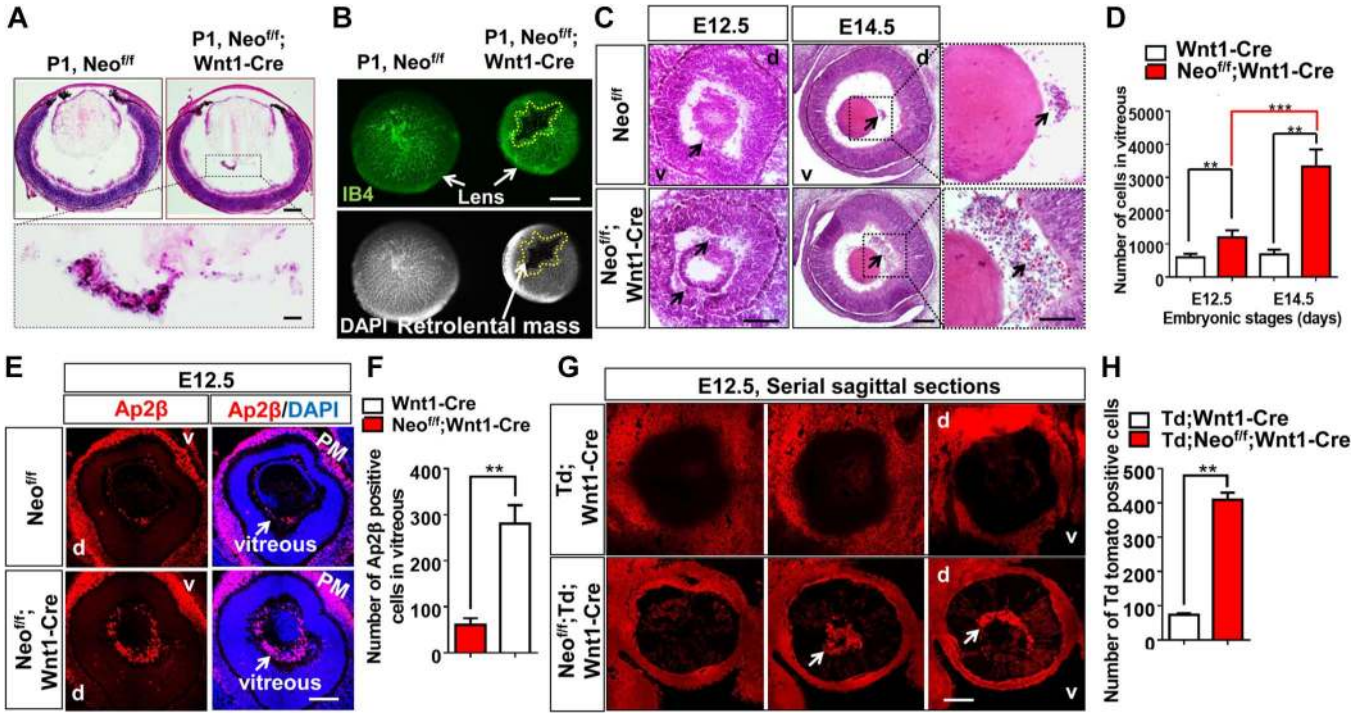

Figure 6 *Neo*$^{f/f}$;*Wnt1*-Cre mice exhibit PHPV phenotype, similar to *Neo*$^{m/m}$ mice. (**A**) Persistent vitreous emergence in the eye of *Neo*$^{f/f}$;*Wnt1*-Cre mice at the P1 stage (H&E staining). Scale bar, 200 μm and 50 μm (enlarged). (**B**) Whole-mount preparation of posterior lens observed in *Neo*$^{f/f}$ and *Neo*$^{f/f}$;*Wnt1*-Cre mice at P1 (IB4 staining, green; DAPI, white). The presence of the retrolental mass is highlighted by the yellow-dotted line. Scale bar, 200 μm. (**C**) Sagittal sections of *Neo*$^{f/f}$ and *Neo*$^{f/f}$;*Wnt1*-Cre eye cup at E12.5 and E14.5 stage. d, dorsal; v, ventral. Scale bar, 100 and 50 μm (enlarged). (**D**) More cells emerged in the vitreous in *Neo*$^{f/f}$;*Wnt1*-Cre eye cup than *Neo*$^{f/f}$ eye cup at E12.5 and E14.5. $n = 6$, $^{**}P < 0.01$. (**E**) Sagittal sections of eye cup showed cells of neural crest origin (Ap2β, red) located in the vitreous in *Neo*$^{f/f}$ and *Neo*$^{f/f}$;*Wnt1*-Cre eye cup at E12.5. Scale bar, 100 μm. (**F**) Quantification of Ap2β-positive cells in the vitreous of *Neo*$^{f/f}$ and *Neo*$^{f/f}$;*Wnt1*-Cre mice. $n = 6$, $^{**}P < 0.01$. (**G**) td labeled cells (NCC origin) emerged in the vitreous, periocular mesenchyme, and neural retina as indicated by serial sagittal sections. *d*, dorsal; *v*, ventral. Scale bar, 100 μm. (**H**) Quantification of Td-positive cells in *Td*$^{f/f}$;*Wnt1*-Cre and *Td*$^{f/f}$;*Neo*$^{f/f}$;*Wnt1*-Cre mice. $n = 6$. $^{**}P < 0.01$. PM, periocular mesenchyme.

mice, showed pigmented retrolental mass in the vitreous after birth by both H&E and IB4 staining analyses (Figure 6A and B). Further examination of their embryos (E12.5 and E14.5) revealed similar phenotypes as that in *Neo*$^{m/m}$ embryos, displaying increased retrolental cell masses (Figure 6C and D). Moreover, these retrolental cell masses were positive for AP2β and *Wnt1*-Cre-driven tdTomato, markers for NCCs, indicating their NCC identity (Figure 6E and G). As quantified, more AP2β immune-positive cells resided in the vitreous of *Neo*$^{f/f}$;*Wnt1*-Cre mice (Figure 6E and F), and more Td-positive cells were found in the vitreous of *Td*$^{f/f}$;*Neo*$^{f/f}$;*Wnt1*-Cre mice (Figure 6H). These results implicate that neogenin in NCCs plays a critical role in NCC delamination/migration/differentiation, and thus preventing PHPV-like deficit.

In addition to *Neo*$^{f/f}$;*Wnt1*-Cre mice, we also crossed *Neo*$^{f/f}$ mice with *GFAP*-Cre and *Nestin*-Cre to generate *Neo*$^{f/f}$;*GFAP*-Cre and *Neo*$^{f/f}$;*Nestin*-Cre, respectively. In both lines, neogenin was knocked out in neural stem cells and astrocytes. In contrast from *Neo*$^{f/f}$;*Wnt1*-Cre mice, both *Neo*$^{f/f}$;*GFAP*-Cre and *Neo*$^{f/f}$;*Nestin*-Cre mutant mice showed no pigmented retrolental masses and no difference in hyaloid vessel density was at ages of P1 and P15 (Supplementary Figure S1), providing additional evidence for neogenin's expression in NCCs, but not in neural stem cells or astrocytes, to be essential for preventing the increased retrolental cell mass.

Increased cell migration in neural crest explant cultures from Neo$^{f/f}$*;Wnt1-Cre embryos*

To test if neogenin expression in NCCs regulates NCC migration in a cell autonomous manner, we cultured neural crest explants from E9 control (*Neo*$^{f/f}$) and *Neo*$^{f/f}$;*Wnt1*-Cre embryos as described previously (Etchevers, 2011). To exclude variation of neural crest explant size, we measured the outgrowth area over original neural crest explant area according to Pryor et al. (2014). A larger NCC migratory area and a greater perimeter of explant were detected in explants from *Neo*$^{f/f}$;*Wnt1*-Cre embryos following 24-h or 48-h cultures (Figure 7A–C). Next, we directly measured the terminal dynamics of cell migration by randomly measuring the distance of NCC leading edges from the center of the explants at 24 h and 48 h DIV. A faster migration rate was found in *Neo*$^{f/f}$;*Wnt1*-Cre group than control group (*Neo*$^{f/f}$) in 24-h and 48-h measurement (Figure 7H), respectively, which

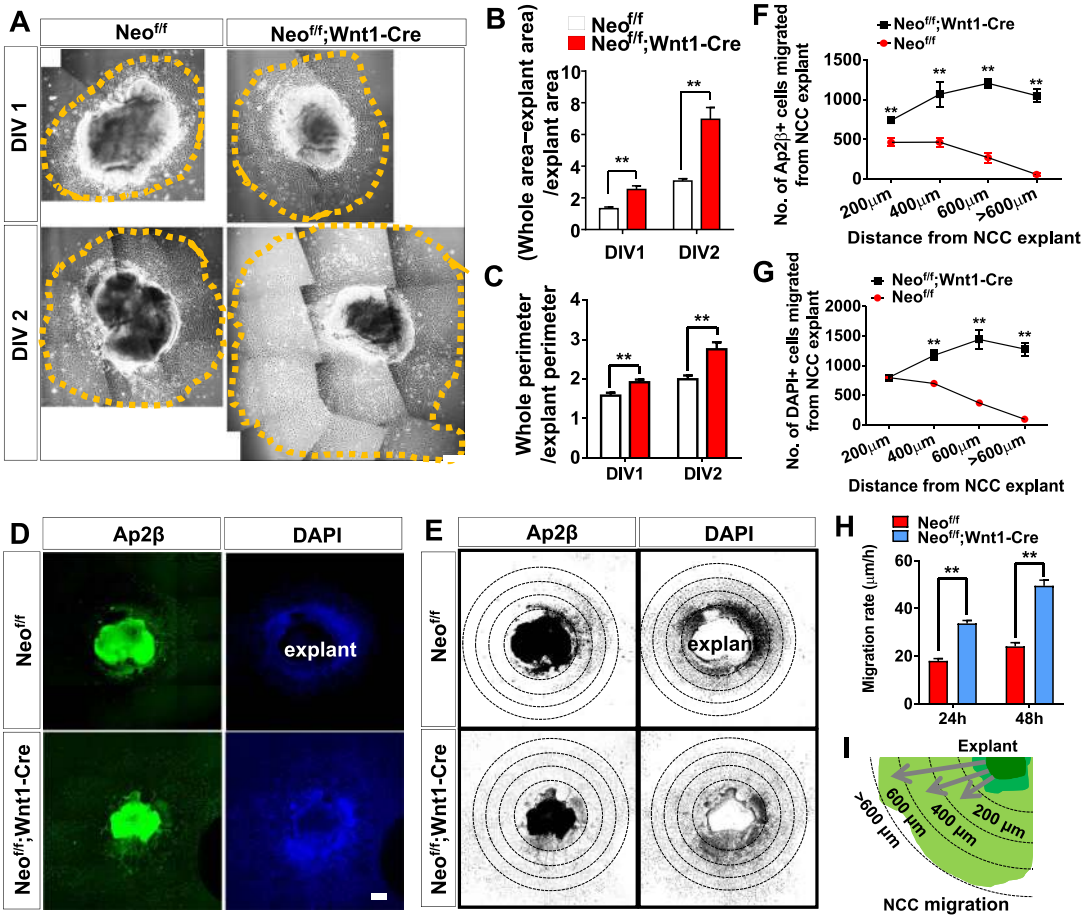

Figure 7 Greater NCC migration from NC explant in the *Neo*$^{f/f}$;*Wnt1*-Cre mice. (**A**) Representative outgrowth of NCCs in *Neo*$^{f/f}$ and *Neo*$^{f/f}$;*Wnt*1-Cre groups at DIV1 and DIV2 (contrast phase). Yellow-dotted line outlines the edge of the NCC explants. Scale bar, 100 μm. (**B**) Quantification of NCC outgrowth area ratio [(whole area – explant area) /explant area]. Data are presented as rate of outgrowth area vs. original NC explant. $^{**}P < 0.01$, $n = 6$. (**C**) Explant perimeter of *Neo*$^{f/f}$;*Wnt1*-Cre group and *Neo*$^{f/f}$ groups. $^{**}P < 0.01$, $n = 6$. (**D**) AP2β was used as an NCC marker to label NC derived cells with DAPI as a nuclear marker. Scale bar, 100 μm. (**E**) Black and white contrast images were isolated from AP2β immunofluorescence and DAPI-positive signals. Dotted circles were used to measure the migration distance of NCCs from the NC explant. (**F**) Quantification of AP2β-positive cells in different circles (200, 400, 600 μm, and above) that migrated from the NC explant. $^{**}P < 0.01$, $n = 6$. (**G**) Quantification of DAPI-positive cells in different circles. $^{**}P < 0.01$, $n = 6$. Student's *t*-test. (**H**) The terminal migration rate quantification of NCCs at 24 h and 48 h in *Neo*$^{f/f}$ and *Neo*$^{f/f}$;*Wnt*1-Cre groups. $^{**}P < 0.01$, $n = 10$. Student's *t*-test within groups. (**I**) Paradigm of NCC migration through different circles. Circles were drawn around the neural crest explant at 200, 400, and 600 μm surrounding the region of interest. Scale bar, 100 μm.

suggested the loss of function of neogenin promotes the NCC migration. The explant cultures were then fixed and immunostained with anti-AP2β to verify the identity of NCCs. Indeed, they were positive for AP2β antibody (Figure 7D and E). In addition, more AP2β-positive and DAPI-positive cells were observed in *Neo*$^{f/f}$;*Wnt1*-Cre cultures as compared with that of *Neo*$^{f/f}$ cultures (Figure 7F and G), supporting the view for increased cell migration in neogenin KO NCCs (Figure 7I).

Delayed retinal fissure closure in both Neo$^{m/m}$ *and Neo*$^{f/f}$*;Wnt1-Cre embryos*

During the process of cellar influx and migration into the embryonic eye cup, the neural retinal fissure closes to form intact morphology of the eye (Heermann et al., 2015). The distal rim of the optic cup is known as the ciliary marginal zone (CMZ) and plays a vital role in fissure formation (Centanin et al., 2011). We thus examined retinal fissure structures. At E11.5, a critical time window for eye cup formation, *Neo*$^{+/+}$ embryos formed an intact retinal fissure along their sagittal plane (Figure 8A). However, *Neo*$^{m/m}$ embryos exhibited a deficit in retinal fissure closure (Figure 8A), which is concurrent with more retrolental cells emerging in the vitreous (Figure 8B). 3D images of eye tissue were used to further assess the fissure deficit (Supplementary 3D video). Moreover, AP2β-positive cells were accumulated between the CMZ region and the vitreous at E11.5 (Supplementary 3D video), and more AP2β-positive

cells emerged in the anterior and posterior eye cup at E12.5 (Supplementary Figure S2). Interestingly, the retinal fissure remained open in *Neo*$^{f/f}$;*Wnt1*-Cre at both E11.5 and E12.5 (Figure 8C; Supplementary Table S2). This deficit was further confirmed by characterizing tdTomator cells in *Neo*$^{f/f}$;*Td*$^{f/f}$;*Wnt1*-Cre and *Td*$^{f/f}$;*Wnt1*-Cre mice (Figure 8D). In Ai9 mice, tdTomato was turned on by *Wnt1*-Cre expression. As shown in Figure 8D–F, the diameter of the fissure structures, the PDGFRβ, and tomato double positive cells within the eye cup were all increased in *Neo*$^{f/f}$;*Td*$^{f/f}$;*Wnt1*-Cre embryos as compared with those in control (*Td*$^{f/f}$;*Wnt1*-Cre) mice (Figure 8E and F). Together, these results suggest that in addition to NCC cell migration, the delayed retinal fissure closure may allow more NCCs migrating into the eye cup, revealing another underlying mechanism for PHPV-like pathology.

Discussion

Although several genetic risk factors have been identified in patients with PHPV (Shirai, 1991; Reichel et al., 1998; Gulati et al., 2003; Mawdsley et al., 2004; Toomes et al., 2004; Junge et al., 2009; Prasov et al., 2012; Son et al., 2014; Salvucci et al., 2015), it remains elusive about the molecular and cellular mechanisms underlying the formation of PHPV. Neogenin is a DCC family receptor, implicated in regulating multiple signals induced by various ligands, including netrins, RGMs, BMPs, and sonic hedgehog (Srinivasan et al., 2003; Lee et al., 2010; Zhou et al., 2010; Hong et al., 2012; Tian et al., 2013; O'Leary et al., 2015; Huang et al., 2016). Here, we provide evidence for neogenin's unrecognized function in regulating PHPV. *Neo*$^{m/m}$ mice develop an unregressed retrolental mass, suggesting a negative role of neogenin in PHPV formation. A high level of neogenin expression in embryonic NCC lineage cells and the PHPV-like deficit detected in *Neo*$^{f/f}$;*Wnt1*-Cre mice suggest a crucial role of neogenin in NCC lineage cells in this pathology. Furthermore, neogenin deficiency increases NCC migration in cultured explants and elevates NCC distribution in the retrolental area. Together, these observations lead us to speculate that neogenin deficiency in NCCs may promote PHPV development by increasing NCC migration.

PHPV is defined as a disease resulting from failed regression of the intraocular vasculature (Goldberg, 1997; Ittner et al., 2005). During embryonic development, the cells in hyaloid vessels and vitreous are derived from the neural crest and mesoderm (Gage et al., 2005). We have found that the retrolental cell mass in *Neo*$^{m/m}$ embryos consists of pericytes, endothelial cells, pigmented cells, and blood cells that originate from the neural crest and the mesoderm, suggesting that the cells in the *Neo*$^{m/m}$ retrolental mass are similar to those found in *Neo*$^{+/+}$ mice, consistent with a previous report (Son et al., 2014). Hyaloid regression occurs in the first few weeks of postnatal development in mice (Saint-Geniez and D'Amore, 2004). In *Neo*$^{m/m}$ pups, hyaloid vasculature in the area outside of the hyperplastic mass was decreased over age, but did not regress until P14 (Figure 2A). These observations suggest that the retrolental mass in neogenin mutant embryos may not be a direct consequence of failed hyaloid vessel regression, but a potential cause of the observed PHPV phenotype. The latter view is also in line with a previous report (Son et al., 2014).

How is the primary vitreous cell mass formed? A greater primary vitreous cell mass was detected ∼E11 *Neo*$^{m/m}$ eye cups (Figure 3; Supplementary 3D video), which failed to be regressed at E16.5 (Figure 3). These observations, in line with the view for human PHPV to be developed during embryonic stages (Gulati et al., 2003), implicate a loss of the restriction of cell migration in developing *Neo*$^{m/m}$ eye. However, these observations cannot eliminate the possibility that increased neural crest progenitors may result in an elevated primary vitreous cell mass. To this end, examining Sox9, FoxD3, and Sox10 early stage NCC markers in control (heterozygotes) and homozygote mutant embryos showed more Sox9^{+} and Sox10^{+} NCC-like cells not only in the mutant retrolental area, but also in the area surrounding the eye discs of ∼E12 mutants (Figure 4J). These results thus suggest that neogenin mutation may affect not only NCC distribution/migration, but also NCC progenitors. However, using proliferative marker, Ki67, we did not observe increased cell proliferation ∼E11 mutant embryos (Figure 3F), but detect an increase in Ki67^{+} cells in ∼E16.5 mutant retrolental area (Figure 3G). These results thus eliminate the possibility for increased NCC progenitors at early stage (e.g. <E10.5) as a major cause for the elevated retrolental cell mass, but the possibility for increased NCCs or NCC progenitors at later stages (e.g. >E12) to contribute to the elevated retrolental cell mass remains.

In addition to cell proliferation, several lines of evidence suggest a role of neogenin in regulating NCC migration, which may underlie the increased retrolental mass in neogenin mutant embryos. First, increased retrolental cell mass was detectable as early as ∼E11 neogenin mutant embryos, which appears to be largely derived from NCC lineage (Figures 3A and 5A). Second, neogenin is highly expressed in NCC lineage cells. Third, neogenin cKO in *Wnt1*-Cre^{+} NCCs showed similar PHPV-like deficit as that of *Neo*$^{m/m}$ mutant mice (Figures 6 and 8). Fourth, the NCC containing explant culture experiments showed increased NCC migration rate in neogenin mutant mice, as compared with that of wild-type control mice (Figure 7).

It is noteworthy that additional mechanisms may underlie neogenin regulation of PHPV pathogenesis. In addition to the increases in NCC migration and NCC progenitors, the unclosed fissure may allow more neural crest-derived cells migrating into the eye cup. Interestingly, neogenin loss-of-function in *Wnt1*-Cre cells also resulted in an unclosed fissure (Figure 8C and D), a similar defect as that of *Neo*$^{m/m}$ embryos. Also of interest to note a report that *Neo*$^{m/m}$ mice show impaired cell adhesions in both ependymal cells and radial glial cells, resulting in a hydrocephalus-like deficit (O'Leary et al., 2017). Thus, it will be of interest to further investigate how neogenin regulates fissure closure, and whether neogenin regulates this event via its regulation of WAVE complex as described in radial glial cells (O'Leary et al., 2017).

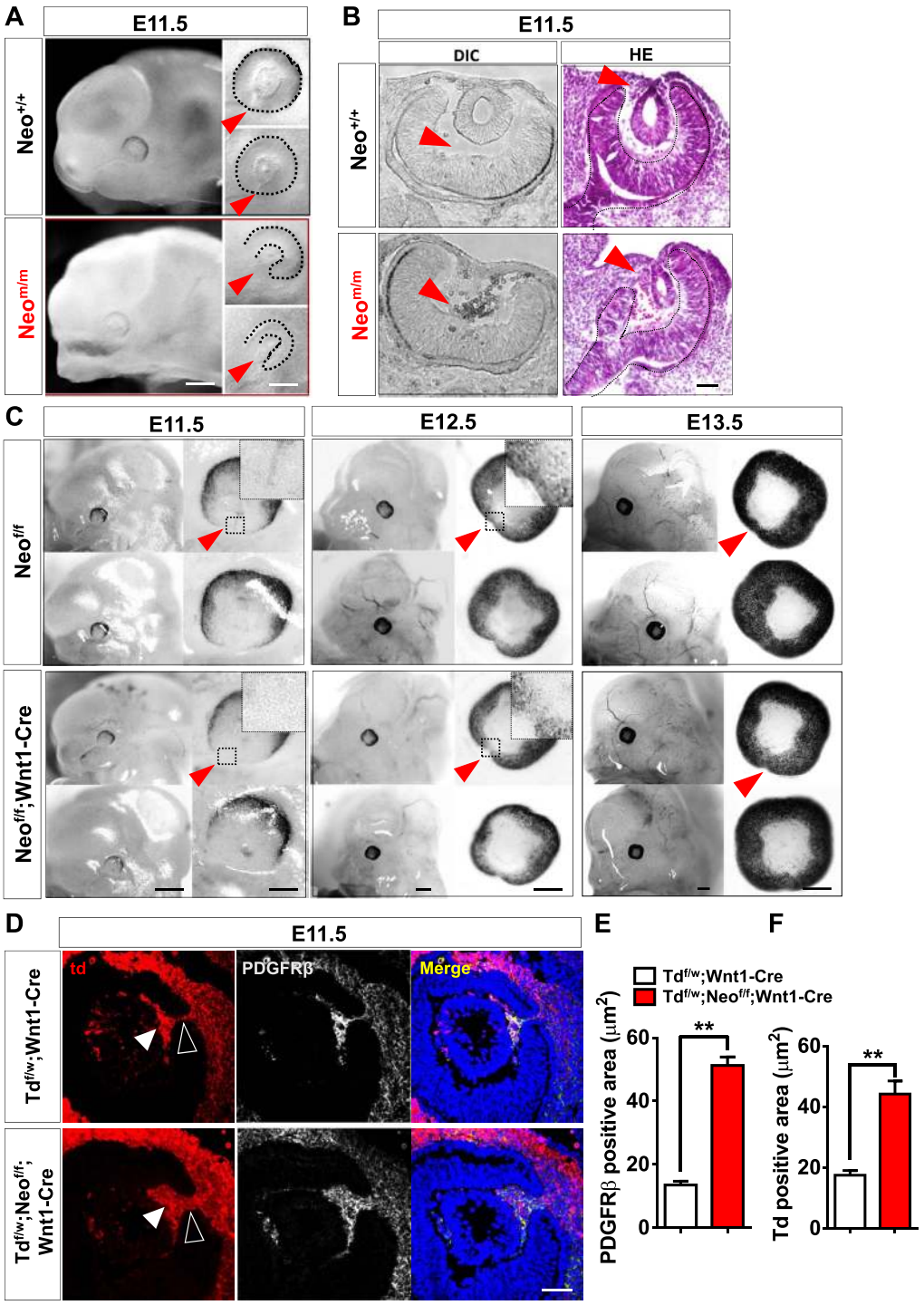

Figure 8 Deficit of ocular fissure closure in the *Neo*$^{m/m}$ eye. (**A**) Head of embryo from E11.5 *Neo*$^{+/+}$ and *Neo*$^{m/m}$ mice (phase image). Fissure in *Neo*$^{+/+}$ eye completely closed and made a circle (right side), but the *Neo*$^{m/m}$ eye cannot form a closed fissure. Black dotted line shows morphology of the eye cup (sagittal view). Scale bar, 500 and 200 μm (enlarged). (**B**) Coronal sections of E11.5 *Neo*$^{+/+}$ and *Neo*$^{m/m}$ mice by DIC scanning and H&E staining. More cells emerged in the vitreous of *Neo*$^{m/m}$ mice. Scale bar, 50 μm. (**C**) Lateral profile of *Neo*$^{f/f}$ and *Neo*$^{f/f}$;*Wnt1*-Cre mice at E11.5, E12.5, and E13.5. Scale bar, 500 and 100μm (enlarged). (**D**) Sagittal sections of *Td*$^{f/f}$;*Wnt1*-Cre and *Td*$^{f/f}$;*Neo*$^{f/f}$;*Wnt1*-Cre eyes co-labeled with PDGFRβ at E11.5. Td (red) labeled cells emerged around the eye cup, into the fissure (open white triangle) and the vitreous (white triangle). Scale bar, 50 μm. (**E**) Larger area of PDGFRβ-positive cells were found in *Td*$^{f/f}$;*Neo*$^{f/f}$;*Wnt1*-Cre mice. (**F**) Td-positive area was larger in *Td*$^{f/f}$;*Neo*$^{f/f}$;*Wnt1*-Cre mice than *Td*$^{f/f}$;*Wnt1*-Cre mice. $n = 6$, $^{**}P < 0.01$. Student's *t*-test.

Materials and methods

Mouse breeding

Neo1 Rosa-26 LacZ transgenic mice were kindly provided by Dr Sue Ackerman (The Jackson Laboratory) as previously described (Lee et al., 2010; Zhou et al., 2010). *Neogenin*$^{f/f}$ (*Neo*$^{f/f}$) mice were generated by Ozgene. *Wnt1*-Cre, *Nestin*-Cre (donated by Dr Rudiger Klein), *GFAP*-Cre and *Ai9* mice (all C57BL/6 genetic background, from Jackson Laboratory) were used and maintained in line with the protocols approved by Augusta University IACUC committee according to US National Institutes of Health guidelines. The *Ai9* mice (stock number 007909), as previously reported (Madisen et al., 2010; Huang et al., 2016), have loxP-flanked STOP cassette preventing transcription of a CAG promoter-driven protein, tdTomato which is expressed following Cre-mediated recombination. Briefly, we first generated *Neo*$^{f/w}$;*X*-Cre. *Neo*$^{f/w}$;*Wnt1*-Cre male mice were then bred with *Neo*$^{f/f}$ female mice to yield 25% *Neo*$^{f/f}$;*Wnt1*-Cre mice and 25% *Neo*$^{f/f}$ mice as littermate controls. These male *Neo*$^{f/f}$;*GFAP*-Cre, *Neo*$^{f/f}$;*Nestin*-Cre mice were obtained by breeding with *Neo*$^{f/f}$ female. *Td*$^{f/f}$;*Neo*$^{f/f}$;*Wnt1*-Cre mice were obtained by breeding *Neo*$^{f/f}$; *Td*$^{f/f}$ mice with *Neo*$^{f/w}$;*Wnt1*-Cre. These mice were confirmed by genotyping using PCR and western blot analysis (Supplementary Figure S3). For embryo generation, embryonic day (E) 0.5 was defined as noon of the day when the vaginal plug was observed.

H&E staining and β-gal detection

H&E staining protocols have been described previously (Liu et al., 2014). Briefly, embryo heads were freshly dissected and sectioned. P0-P30 dissected eyes were prepared in 4% formaldehyde fixation solution at 4°C overnight, dehydrated the following day in 30% sucrose, and embedded in OCT (Sakura). Sections were stained with H&E solution (Sigma-Aldrich), followed by alcohol dehydration and xylene permeability.

β-Gal activity was detected as described previously (Liu et al., 2014). In brief, frozen eye sections derived from *Neo*$^{+/+}$ and *Neo*$^{m/m}$ mice were fixed with 1.5% glutaraldehyde plus 0.5% Paraformaldehyde and incubated with X-gal solution (2 mM $MgCl_2$, 5 mM potassium ferricyanide, 5 mM potassium ferrocyanide, and 0.1% X-gal) in the dark at 37°C for 30 min. The slides were then washed twice and co-stained with fast red (Vector) and were mounted using permount (Thermo Fisher Scientific). Images were taken by microscope with high sensitivity CCD (AxioCam, Carl Zeiss).

Immuno- and histo-staining

Embryo heads (E10.5–E16.5) were freshly dissected, cryopreserved in OCT compound, and sectioned along the coronal and sagittal plane, followed by 4% formaldehyde fixation solution at 4°C for 1 h. A total of 16–18 μm embryonic tissue sections were then processed for immunostaining by phosphate buffered saline (PBS) rinse, blocked for 1 h in 5% BSA plus 0.1% triton at room temperature (RT), incubated with primary antibodies overnight at 4°C, followed by 1 h incubation at RT with fluorescence-conjugated secondary antibodies (Jackson Laboratory). The slides were mounted using DAPI mounting medium (Vector). The primary antibodies used in the experiments were anti-PH3 (1:500, Millipore), anti-Ki67 (1:400, Millipore), anti-MiTF (1:400, Abcam), anti-AP2β (1:300, Cell Signaling Technology), anti-CD31 (1:500, BD), anti-PDGFRβ (1:500, Abcam), anti-Sox9 (1:300, Millipore), anti-FoxD3 (1:300, Cell Signaling Technology), and anti-Sox10 (1:300, Cell Signaling Technology). Hyaloid vessels and retinal vessels were stained using fluorescein isolectin B4 (1:500, Vector Laboratories) at 4°C overnight. DAPI (Sigma and Vector Laboratories) was used for nuclear staining.

Neural crest explants primary culture

E9 embryos were dissected from *Neo*$^{f/w}$;*Wnt1*-Cre pregnant mice in ice cold PBS according to Etchevers (2011). After removal of the heart tube and the pharyngeal arches, transverse cuts were made just posterior to the optic vesicles, through the diencephalon. Cranial tissue was digested in 2% pancreatin (Sigma) for 15 min at RT, and the digested tissue was plated onto Metrixgel (BD)-coated cover glasses. Cranial NCC explants were cultured at 37°C (5% CO_2/95% air) for 0–48 h in complete NCC culture medium supplied with hydrocortisone, transferrin, triiodothyronine (T3), glucagon, insulin, epidermal growth factor, and fibroblast growth factor, plus 1% penicillin and streptomycin. Before staining, explants were fixed for 10 min with 4% PFA.

Analysis of NCC migration in vitro

Cell migration over 2 days was assessed by measuring the percentage of increased area and perimeter as described (Pryor et al., 2014), taking into account any variation due to different original size of the neural crest explant.

$$\text{Cell migration evaluation} = \frac{\text{(The whole area and perimeter of outgrowth} - \text{area and perimeter of original explant)}}{\text{area and perimeter of original explant}}$$

Migration rate was analyzed by measuring the distance traveled by AP2β-positive cells beyond 200, 400, 600 μm, and above at 24-h and 48-h cultures according to Richardson et al. (2016) with minor modifications. Briefly, extent of chain and cell outgrowth using a scale that originates from the center of the explant. Random cellular extensions (8 chains in each explant) were quantified and averaged from six independent explants.

$$\text{Cell migration rate } (\mu m/h) = \frac{\text{Average distances of migrated cells from the center of the explant}}{\text{Migration time}}$$

Migration rate and distance analysis were made on at least six neural crest explants for each genotype. All areas, perime-

ter, and distance measurements were performed using Image J software (NIH).

Western blotting

Brain tissues and eye samples were lyzed in lysis buffer (50 mM Tris-HCl, pH 7.4, 150 mM NaCl, 1% NP-40, 0.5% Triton X-100, 1 mM phenylmethylsulfonyl fluoride, 1 mM EDTA, 5 mM sodium fluoride, 2 mM sodium orthovanadate, and protease inhibitor cocktail) for 30 min on ice and centrifuged at 12000 *g* for 20 min. The concentration of protein lysate was determined using a bicinchoninic acid (BCA) protein assay kit (Bio-rad). Proteins were separated by 8%–10% sodium dodecyl sulphate-polyacrylamide gel electrophoresis gel electrophoresis and electro-transferred onto the nitrocellulose membrane and were then blocked in 5% skim milk at RT for 1 h and incubated with primary antibody overnight at 4°C. Membranes were rinsed on the next day, followed by 1 h incubation (RT) with an appropriate horseradish peroxidase-conjugated secondary antibody (1:5000, Thermo). Chemiluminescent detection was performed with the ECL kit (Pierce). Rabbit polyclonal anti-neogenin was generated as described previously (Xie et al., 2005), using the GST-C-terminus of neogenin fusion protein as the antigen. β-Actin (1:10000, Sigma) was detected alongside the experimental samples as a loading control.

Whole-mount hyaloid preparation

WT and *Neo*$^{f/f}$, *Neo*$^{f/f}$;*GFAP*-Cre, *Neo*$^{f/f}$;*Wnt1*-Cre, *Neo*$^{f/f}$;*Nestin*-Cre eyes were enucleated and their corneas removed from P1, P7, and P15 mice. The dissected eyes were fixed for 2 h in 4% paraformaldehyde on ice, after which the eyes were rinsed in PBS. The retinal cup along with the lenses then was removed from the sclera carefully, after which the retina was dissected apart from the posterior pole with the intact hyaloid vessels attached to the lens. Lenses with the hyaloid network were stained by FITC-conjugated isolectin-B4 mixed with phosphate buffered solution with 0.1% triton (PBST) overnight (1:400, FL-1201; Vector Laboratories) and mounted in DAPI medium (H-1200, Vector Laboratories). Z-stack images were taken using a Zeiss confocal microscope system LSM510. Density of hyaloid vessels was quantified as the ratio (%) of area of hyaloid vessels vs. the posterior lens area by an Angio tool software (NIH/NCI). Quantification of vessels the tunica vasculosa lentis was modified from that have been described previously (Ito and Yoshioka, 1999). Briefly, an equator of the lens was drawn on the posterior lens, and vessels crossing this line were counted by Angio tool software (below). By confocal scanning, we could obtain all the z-stack layers from the half lens with hyaloid vessels. For immune-labeled cells, 6–8 tissue blocks from 3–4 mice (two blocks per mouse) were taken from each group. Immune-positive signals were quantified (2–3 measurements per tissue block, 4–6 animals per group).

Statistical analysis

All data presented represent results from at least three independent experiments. Statistical analysis was performed using Student's *t*-test or ANOVA with pair-wise comparisons. Statistical significance was defined as $P < 0.05$.

Supplementary material

Supplementary material is available at *Journal of Molecular Cell Biology* online.

Acknowledgements

We thank Xiong and Mei's lab members for discussion and data evaluation.

Funding

This study was supported in part by grants from the National Institutes of Health (NIH AG045781) to W.-C.X.

Conflict of interest: none declared.

Author contributions: W.-C.X. and S.L. designed experiments and interpreted results; S.L., W.L., C.-L.C., D.S., and J.-X.H. performed experiments and analyzed data; W.-C.X. and S.L. wrote the manuscript; L.M., L.L., and J.Y. helped evaluate the data and revise the manuscript.

References

Anteby, I., Cohen, E., Karshai, I., et al. (2002). Unilateral persistent hyperplastic primary vitreous: course and outcome. J. AAPOS *6*, 92–99.

Barishak, Y.R. (1992). Embryology of the eye and its adnexae. Dev. Ophthalmol. *24*, 1–142.

Beauchamp, G.R., and Knepper, P.A. (1984). Role of the neural crest in anterior segment development and disease. J. Pediatr. Ophthalmol. Strabismus *21*, 209–214.

Brault, V., Moore, R., Kutsch, S., et al. (2001). Inactivation of the β-catenin gene by Wnt1-Cre-mediated deletion results in dramatic brain malformation and failure of craniofacial development. Development *128*, 1253–1264.

Centanin, L., Hoeckendorf, B., and Wittbrodt, J. (2011). Fate restriction and multipotency in retinal stem cells. Cell Stem Cell *9*, 553–562.

Chen, C.L., Broom, D.C., Liu, Y., et al. (2006). Runx1 determines nociceptive sensory neuron phenotype and is required for thermal and neuropathic pain. Neuron *49*, 365–377.

Cooper, M.A., Son, A.I., Komlos, D., et al. (2008). Loss of ephrin-A5 function disrupts lens fiber cell packing and leads to cataract. Proc. Natl Acad. Sci. USA *105*, 16620–16625.

De Vries, M., and Cooper, H.M. (2008). Emerging roles for neogenin and its ligands in CNS development. J. Neurochem. *106*, 1483–1492.

Etchevers, H. (2011). Primary culture of chick, mouse or human neural crest cells. Nat. Protoc. *6*, 1568–1577.

Freeman-Anderson, N.E., Zheng, Y., McCalla-Martin, A.C., et al. (2009). Expression of the Arf tumor suppressor gene is controlled by Tgfβ2 during development. Development *136*, 2081–2089.

Gage, P.J., Rhoades, W., Prucka, S.K., et al. (2005). Fate maps of neural crest and mesoderm in the mammalian eye. Invest. Ophthalmol. Vis. Sci. *46*, 4200–4208.

Goldberg, M.F. (1997). Persistent fetal vasculature (PFV): an integrated interpretation of signs and symptoms associated with persistent hyperplastic primary vitreous (PHPV). LIV Edward Jackson Memorial Lecture. Am. J. Ophthalmol. *124*, 587–626.

Gulati, N., Eagle, R.C., Jr, and Tasman, W. (2003). Unoperated eyes with persistent fetal vasculature. Trans. Am. Ophthalmol. Soc. *101*, 59–65.

Hackett, S.F., Wiegand, S., Yancopoulos, G., et al. (2002). Angiopoietin-2 plays an important role in retinal angiogenesis. J. Cell. Physiol. *192*, 182–187.

Haddad, R., Font, R.L., and Reeser, F. (1978). Persistent hyperplastic primary vitreous. A clinicopathologic study of 62 cases and review of the literature. Surv. Ophthalmol. *23*, 123–134.

Hahn, P., Lindsten, T., Tolentino, M., et al. (2005). Persistent fetal ocular vasculature in mice deficient in bax and bak. Arch. Ophthalmol. *123*, 797–802.

Heermann, S., Schutz, L., Lemke, S., et al. (2015). Eye morphogenesis driven by epithelial flow into the optic cup facilitated by modulation of bone morphogenetic protein. eLife *4*, e05216.

Hong, M., Schachter, K.A., Jiang, G., et al. (2012). Neogenin regulates sonic Hedgehog pathway activity during digit patterning. Dev. Dyn. *241*, 627–637.

Huang, Z., Sun, D., Hu, J.X., et al. (2016). Neogenin promotes BMP2 activation of YAP and Smad1 and enhances astrocytic differentiation in developing mouse neocortex. J. Neurosci. *36*, 5833–5849.

Hunt, A., Rowe, N., Lam, A., et al. (2005). Outcomes in persistent hyperplastic primary vitreous. Br. J. Ophthalmol. *89*, 859–863.

Ito, M., and Yoshioka, M. (1999). Regression of the hyaloid vessels and pupillary membrane of the mouse. Anat. Embryol. *200*, 403–411.

Ittner, L.M., Wurdak, H., Schwerdtfeger, K., et al. (2005). Compound developmental eye disorders following inactivation of TGFβ signaling in neural-crest stem cells. J. Biol. *4*, 11.

Johnston, M.C., Noden, D.M., Hazelton, R.D., et al. (1979). Origins of avian ocular and periocular tissues. Exp. Eye Res. *29*, 27–43.

Jun, G., Guo, H., Klein, B.E., et al. (2009). EPHA2 is associated with age-related cortical cataract in mice and humans. PLoS Genet. *5*, e1000584.

Junge, H.J., Yang, S., Burton, J.B., et al. (2009). TSPAN12 regulates retinal vascular development by promoting Norrin- but not Wnt-induced FZD4/β-catenin signaling. Cell *139*, 299–311.

Kelsh, R.N. (2006). Sorting out Sox10 functions in neural crest development. Bioessays *28*, 788–798.

Kheir, V., Munier, F.L., Aubry-Rozier, B., et al. (2016). Potential blindness in children of patients with hereditary bone disease. Osteoporos. Int. *27*, 841–844.

Kim, J., Lo, L., Dormand, E., et al. (2003). SOX10 maintains multipotency and inhibits neuronal differentiation of neural crest stem cells. Neuron *38*, 17–31.

Kulesa, P., Ellies, D.L., and Trainor, P.A. (2004). Comparative analysis of neural crest cell death, migration, and function during vertebrate embryogenesis. Dev. Dyn. *229*, 14–29.

Le Douarin, N. (1980). Migration and differentiation of neural crest cells. Curr. Top. Dev. Biol. *16*, 31–85.

Lee, D.H., Zhou, L.J., Zhou, Z., et al. (2010). Neogenin inhibits HJV secretion and regulates BMP-induced hepcidin expression and iron homeostasis. Blood *115*, 3136–3145.

Liu, W., Tang, F.L., Erion, J., et al. (2014). Vps35 haploinsufficiency results in degenerative-like deficit in mouse retinal ganglion neurons and impairment of optic nerve injury-induced gliosis. Mol. Brain *7*, 10.

Madisen, L., Zwingman, T.A., Sunkin, S.M., et al. (2010). A robust and high-throughput Cre reporting and characterization system for the whole mouse brain. Nat. Neurosci. *13*, 133–140.

Martin, A.C., Thornton, J.D., Liu, J., et al. (2004). Pathogenesis of persistent hyperplastic primary vitreous in mice lacking the arf tumor suppressor gene. Invest. Ophthalmol. Vis. Sci. *45*, 3387–3396.

Matsubara, A., Ozeki, H., Matsunaga, N., et al. (2001). Histopathological examination of two cases of anterior staphyloma associated with Peters' anomaly and persistent hyperplastic primary vitreous. Br. J. Ophthalmol. *85*, 1421–1425.

Mawdsley, D.J., Cooper, H.M., Hogan, B.M., et al. (2004). The Netrin receptor Neogenin is required for neural tube formation and somitogenesis in zebrafish. Dev. Biol. *269*, 302–315.

McGannon, P., Miyazaki, Y., Gupta, P.C., et al. (2006). Ocular abnormalities in mice lacking the ski proto-oncogene. Invest. Ophthalmol. Vis. Sci. *47*,4231–4237.

McKeller, R.N., Fowler, J.L., Cunningham, J.J., et al. (2002). The Arf tumor suppressor gene promotes hyaloid vascular regression during mouse eye development. Proc. Natl Acad. Sci. USA *99*, 3848–3853.

Monnier, P.P., Sierra, A., Macchi, P., et al. (2002). RGM is a repulsive guidance molecule for retinal axons. Nature *419*, 392–395.

Mori-Akiyama, Y., Akiyama, H., Rowitch, D.H., et al. (2003). Sox9 is required for determination of the chondrogenic cell lineage in the cranial neural crest. Proc. Natl Acad. Sci. USA *100*, 9360–9365.

O'Leary, C.J., Bradford, D., Chen, M., et al. (2015). The Netrin/RGM receptor, Neogenin, controls adult neurogenesis by promoting neuroblast migration and cell cycle exit. Stem Cells *33*, 503–514.

O'Leary, C.J., Nourse, C.C., Lee, N.K., et al. (2017). Neogenin recruitment of the WAVE regulatory complex to ependymal and radial progenitor adherensjunctions prevents hydrocephalus. Cell Rep. *20*, 370–383.

Pollard, Z.F. (1997). Persistent hyperplastic primary vitreous: diagnosis, treatment and results. Trans. Am. Ophthalmol. Soc. *95*, 487–549.

Prasov, L., Masud, T., Khaliq, S., et al. (2012). ATOH7 mutations cause autosomal recessive persistent hyperplasia of the primary vitreous. Hum. Mol. Genet. *21*, 3681–3694.

Pryor, S.E., Massa, V., Savery, D., et al. (2014). Vangl-dependent planar cell polarity signalling is not required for neural crest migration in mammals. Development *141*, 3153–3158.

Rajagopalan, S., Deitinghoff, L., Davis, D., et al. (2004). Neogenin mediates the action of repulsive guidance molecule. Nat. Cell Biol. *6*, 756–762.

Reichel, M.B., Ali, R.R., D'Esposito, F., et al. (1998). High frequency of persistent hyperplastic primary vitreous and cataracts in p53-deficient mice. Cell Death Differ. *5*, 156–162.

Richardson, J., Gauert, A., Briones Montecinos, L., et al. (2016). Leader cells define directionality of trunk, but not cranial, neural crest cell migration. Cell Rep. *15*, 2076–2088.

Rizvi, S.W., Siddiqui, M.A., Khan, A.A., et al. (2013). Bilateral persistent hyperplastic primary vitreous: a close mimic of retinoblastoma. Semin. Ophthalmol. *28*, 25–27.

Saint-Geniez, M., and D'Amore, P.A. (2004). Development and pathology of the hyaloid, choroidal and retinal vasculature. Int. J. Dev. Biol. *48*, 1045–1058.

Salvucci, O., Ohnuki, H., Maric, D., et al. (2015). EphrinB2 controls vessel pruning through STAT1–JNK3 signalling. Nat. Commun. *6*, 6576.

Sanghvi, D.A., Sanghvi, C.A., and Purandare, N.C. (2005). Bilateral persistent hyperplastic primary vitreous. Australas. Radiol. *49*, 72–74.

Schnichels, S., Conrad, S., Warstat, K., et al. (2007). Gene expression of the repulsive guidance molecules/neogenin in the developing and mature mouse visual system: C57BL/6J vs. the glaucoma model DBA/2J. Gene Expr. Patterns *8*, 1–11.

Shastry, B.S. (2009). Persistent hyperplastic primary vitreous: congenital malformation of the eye. Clin. Experiment. Ophthalmol. *37*, 884–890.

Shirai, S. (1991). Developmental mechanisms of congenital eye abnormalities. Nippon Ganka Gakkai Zasshi *95*, 1206–1237.

Son, A.I., Sheleg, M., Cooper, M.A., et al. (2014). Formation of persistent hyperplastic primary vitreous in ephrin-A5$^{-/-}$ mice. Invest. Ophthalmol. Vis. Sci. *55*, 1594–1606.

Srinivasan, K., Strickland, P., Valdes, A., et al. (2003). Netrin-1/neogenin interaction stabilizes multipotent progenitor cap cells during mammary gland morphogenesis. Dev. Cell *4*, 371–382.

Sun, D., Sun, X.D., Zhao, L., et al. (2018). Neogenin, a regulator of adult hippocampal neurogenesis, prevents depressive-like behavior. Cell Death Dis. *9*, 8.

Taylor, M.K., Yeager, K., and Morrison, S.J. (2007). Physiological notch signaling promotes gliogenesis in the developing peripheral and central nervous systems. Development *134*, 2435–2447.

Teng, L., Mundell, N.A., Frist, A.Y., et al. (2008). Requirement for Foxd3 in the maintenance of neural crest progenitors. Development *135*, 1615–1624.

Thornton, J.D., Swanson, D.J., Mary, M.N., et al. (2007). Persistent hyperplastic primary vitreous due to somatic mosaic deletion of the arf tumor suppressor. Invest. Ophthalmol. Vis. Sci. *48*, 491–499.

Tian, C., Shi, H., Xiong, S., et al. (2013). The neogenin/DCC homolog UNC-40 promotes BMP signaling via the RGM protein DRAG-1 in C. elegans. Development *140*, 4070–4080.

Toomes, C., Bottomley, H.M., Jackson, R.M., et al. (2004). Mutations in LRP5 or FZD4 underlie the common familial exudative vitreoretinopathy locus on chromosome 11q. Am. J. Hum. Genet. *74*, 721–730.

Wang, W.D., Melville, D.B., Montero-Balaguer, M., et al. (2011). Tfap2a and Foxd3 regulate early steps in the development of the neural crest progenitor population. Dev. Biol. *360*, 173–185.

Wilson, N.H., and Key, B. (2006). Neogenin interacts with RGMa and netrin-1 to guide axons within the embryonic vertebrate forebrain. Dev. Biol. *296*, 485–498.

Xie, Y., Ding, Y.Q., Hong, Y., et al. (2005). Phosphatidylinositol transfer protein-alpha in netrin-1-induced PLC signalling and neurite outgrowth. Nat. Cell Biol. *7*, 1124–1132.

Xu, K., Wu, Z., Renier, N., et al. (2014). Neural migration. Structures of netrin-1 bound to two receptors provide insight into its axon guidance mechanism. Science *344*, 1275–1279.

Zhang, J., Fuhrmann, S., and Vetter, M.L. (2008). A nonautonomous role for retinal frizzled-5 in regulating hyaloid vitreous vasculature development. Invest. Ophthalmol. Vis. Sci. *49*, 5561–5567.

Zhou, Z., Xie, J., Lee, D., et al. (2010). Neogenin regulation of BMP-induced canonical Smad signaling and endochondral bone formation. Dev. Cell *19*, 90–102.

Zhu, M., Provis, J.M., and Penfold, P.L. (1999). The human hyaloid system: cellular phenotypes and inter-relationships. Exp. Eye Res. *68*, 553–563.